Rac1 functions as a reversible tension modulator to stabilize VE-cadherin trans-interaction

Nazila Daneshjou,[1] Nathan Sieracki,[1] Geerten P. van Nieuw Amerongen,[1,2] Daniel E. Conway,[4] Martin A. Schwartz,[3] Yulia A. Komarova,[1] and Asrar B. Malik[1]

[1]Department of Pharmacology, University of Illinois College of Medicine, Chicago, IL 60612
[2]Department of Physiology, Institute for Cardiovascular Research, Vrije University of Amsterdam, 1081 HV Amsterdam, Netherlands
[3]Department of Cell Biology, Yale University School of Medicine, New Haven, CT 06510
[4]Department of Biomedical Engineering, Virginia Commonwealth University, Richmond, VA 23284

The role of the RhoGTPase Rac1 in stabilizing mature endothelial adherens junctions (AJs) is not well understood. In this paper, using a photoactivatable probe to control Rac1 activity at AJs, we addressed the relationship between Rac1 and the dynamics of vascular endothelial cadherin (VE-cadherin). We demonstrated that Rac1 activation reduced the rate of VE-cadherin dissociation, leading to increased density of VE-cadherin at AJs. This response was coupled to a reduction in actomyosin-dependent tension across VE-cadherin adhesion sites. We observed that inhibiting myosin II directly or through photo-release of the caged Rho kinase inhibitor also reduced the rate of VE-cadherin dissociation. Thus, Rac1 functions by stabilizing VE-cadherin trans-dimers in mature AJs by counteracting the actomyosin tension. The results suggest a new model of VE-cadherin adhesive interaction mediated by Rac1-induced reduction of mechanical tension at AJs, resulting in the stabilization of VE-cadherin adhesions.

Introduction

The vascular endothelial cadherin (VE-cadherin)–mediated adherens junction (AJ) complex is the primary restrictive barrier of the endothelium to plasma proteins and blood cells (Giannotta et al., 2013). The VE-cadherin extracellular domain undergoes trans-homodimerization after cell–cell contact (Zhang et al., 2009; Brasch et al., 2011). Stabilization of adhesions requires attachment of the cadherin intracellular domain via catenins to the actin cytoskeleton (Baumgartner et al., 2003; Hong et al., 2013). Cadherin "outside-in" signaling orchestrated by the opposing actions of RhoGTPases Rac1 and RhoA is responsible for remodeling of the actin cytoskeleton at the nascent adhesion sites (Noren et al., 2001; Lampugnani et al., 2002; Cain et al., 2010). In epithelial cells, spatiotemporal activity of Rac1 induced polymerization of actin filaments at the cadherin complex (Ehrlich et al., 2002) to initiate cell–cell contact (Yamada and Nelson, 2007), whereas RhoA activity at the contact sites mediated actomyosin-dependent expansion of the adhesion zone (Yamada and Nelson, 2007).

The role of Rac1 at mature cell–cell adhesions in endothelial cells, which mediate the AJ barrier function, is not well understood. Activation of Rac1 can induce a range of responses from stabilization of endothelial AJs on exposure to shear stress or barrier-enhancing mediators, such as sphingosine-1-phosphate (Lee et al., 1999; Mehta et al., 2005; Liu et al., 2013), to disassembly of AJs in response to vascular endothelial growth factor and tumor necrosis factor (van Wetering et al., 2002; Eriksson et al., 2003; Monaghan-Benson and Burridge, 2009; Naikawadi et al., 2012). A likely explanation for this variability is that global Rac1 activation is often accompanied by mobilization of other signaling pathways that modify localized responses at AJs (Komarova and Malik, 2010; Spindler et al., 2010). Most means of Rac1 activation involve activating the GTPase in the cell, and as such, local Rac1-mediated signaling events are not detected or masked by divergent signals. Here, using the photoactivatable (PA) probe bearing the constitutively active $Rac1^{V12}$ mutant (Wu

Correspondence to Asrar B. Malik: abmalik@uic.edu; or Yulia A. Komarova: ykomarov@uic.edu

Abbreviations used in this paper: AJ, adherens junction; CMV, cytomegalovirus; cRO, caged Rockout; DN, dominant negative; FRET, Förster resonance energy transfer; GAP, GTPase-activating protein; HMEC, human dermal microvascular endothelial cell; MLCII, myosin-II light chain; NMR, nuclear magnetic resonance; PA, photoactivatable; PI, photoinsensitive; ROCK, Rho-associated protein kinase; VE-cadherin, vascular endothelial cadherin.

The Rockefeller University Press $30.00
J. Cell Biol. Vol. 208 No. 1 23–32
www.jcb.org/cgi/doi/10.1083/jcb.201409108

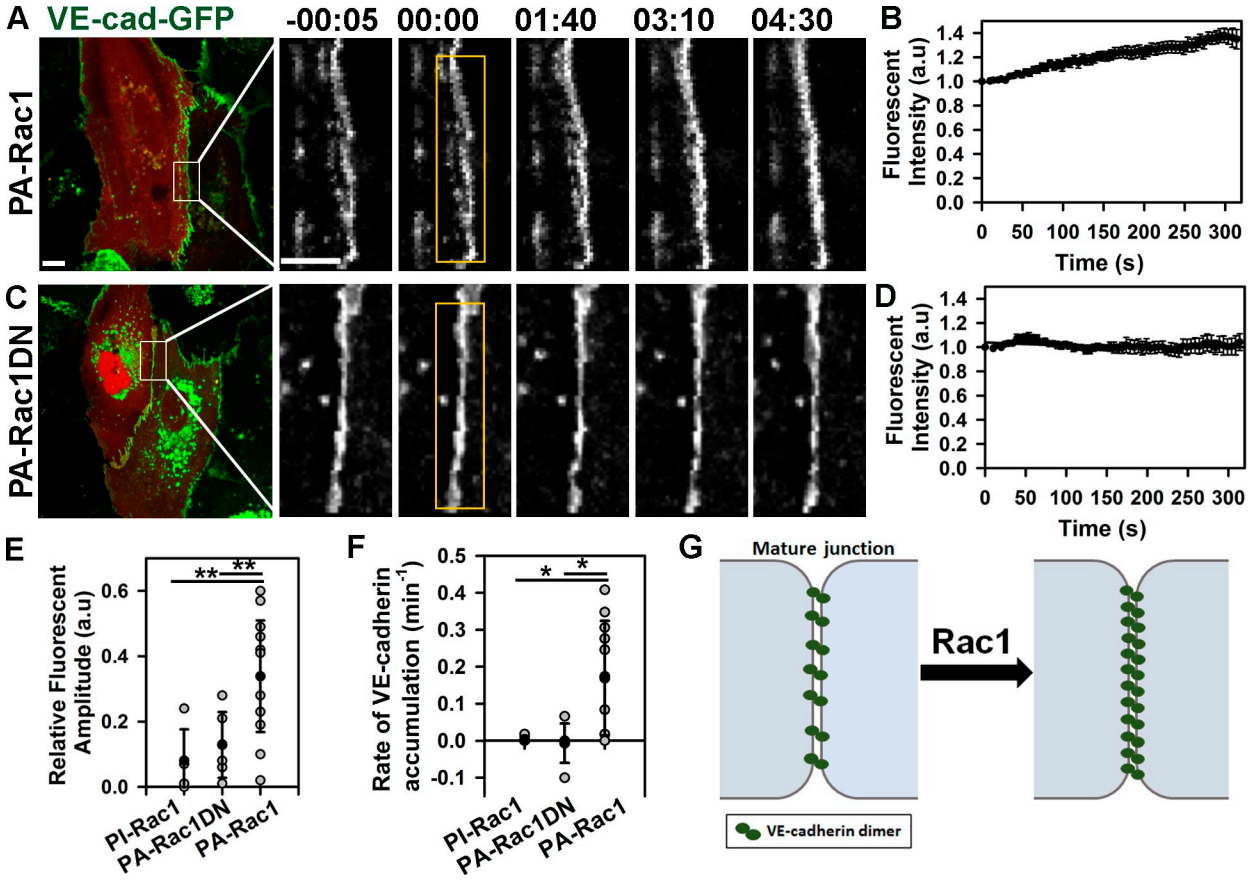

Figure 1. **Photoactivation of Rac1 at AJs increases VE-cadherin density.** (A and C) Time-lapse images of VE-cadherin–GFP (VE-cad-GFP) in cells expressing either mCherry-tagged PA-Rac1 (A) or PA-Rac1DN (C) before and after photoactivation inside the yellow rectangular region at time 0. Time in minutes and seconds is shown. Bars: (main images) 10 µm (insets) 5 µm. (B and D) Relative changes in VE-cadherin–GFP fluorescence intensity at AJs within activation zone for PA-Rac1 (B) or PA-Rac1DN (D) as shown in A and C; means ± SEM, n = 6–14. (E) Amplitude of VE-cadherin–GFP accumulation after activation of PI-Rac1 (0.08 ± 0.1), PA-Rac1DN (0.13 ± 0.1), or PA-Rac1 (0.34 ± 0.17); means ± SD, n = 5–14; *, P < 0.005. (F) The rate constant for VE-cadherin–GFP accumulation after activation of PA-Rac1 was 0.17 ± 0.16 min^{-1}, whereas no significant change was observed with PI-Rac1 or PA-Rac1DN; means ± SD, n = 5–11; *, P < 0.05. (G) Model demonstrating the relationship between Rac1 activity and VE-cadherin density at mature AJs. a.u., arbitrary unit.

et al., 2009), we investigated the role of spatiotemporal Rac1 activity in regulating VE-cadherin dynamics in mature AJs of confluent endothelial monolayers.

Results and discussion

Photoactivation of PA-Rac1 with a 458-nm laser beam occurring with a half-life of ∼25 s mimicked the transient endogenous Rac1 activation induced by sphingosine-1-phosphate (Lee et al., 1999; Mehta et al., 2005; Yamada and Nelson, 2007). We observed that activation of PA-Rac1 in different endothelial cell types induced VE-cadherin accumulation within the photoactivation zone (Fig. 1, A–F; and Fig. S1, A–D). The increased VE-cadherin density, however, was not accompanied by expansion of adhesion zone (Fig. S1 E), suggesting that any effect of lamellipodia activity was negligible. In contrast, activation of control photoinsensitive (PI) Rac1 (PI-Rac1) or a probe bearing a dominant-negative (DN) $Rac1^{T17}$ mutant (PA-Rac1DN; Wu et al., 2009) had no effect on VE-cadherin density at AJs (Fig. 1, C–F). These results showed that spatiotemporal activation of Rac1 at mature AJs functioned by increasing VE-cadherin density of the junctions (Fig. 1 G).

Cadherin-mediated adhesion is a dynamic event characterized by continuous rearrangements of cadherin adhesive bonds (Hong et al., 2011), lateral movement of cadherin within AJs (Baumgartner et al., 2003), and exchange of cadherin between junctional and intracellular pools (de Beco et al., 2009; Hong et al., 2010). To determine how Rac1 regulated VE-cadherin assembly at AJs, we tagged VE-cadherin to the photoswitchable fluorescent protein Dendra2, which exhibits a shift in emission spectrum from a 488- to 543-nm maximum wavelength after photoconversion (Chudakov et al., 2007). VE-cadherin–Dendra2 was used because irradiation with the 458-nm laser beam required for PA-Rac1 activation did not interfere with photoconversion of Dendra2 (Fig. S2 A). Thus, VE-cadherin behavior at AJs as determined from the kinetics of fluorescent recovery at 488 nm defined the association of new VE-cadherin molecules to the AJs, whereas fluorescent decay at 543 nm described the net effect of VE-cadherin lateral movement and dissociation from AJs (Fig. 2 A). We observed that VE-cadherin lateral movement contributed little to the decay kinetics (Fig. S2 B). However, VE-cadherin underwent rapid exchange between the junctional and intracellular pools (Fig. 2, E and G). PA-Rac1 activation significantly reduced the rate constant of VE-cadherin dissociation

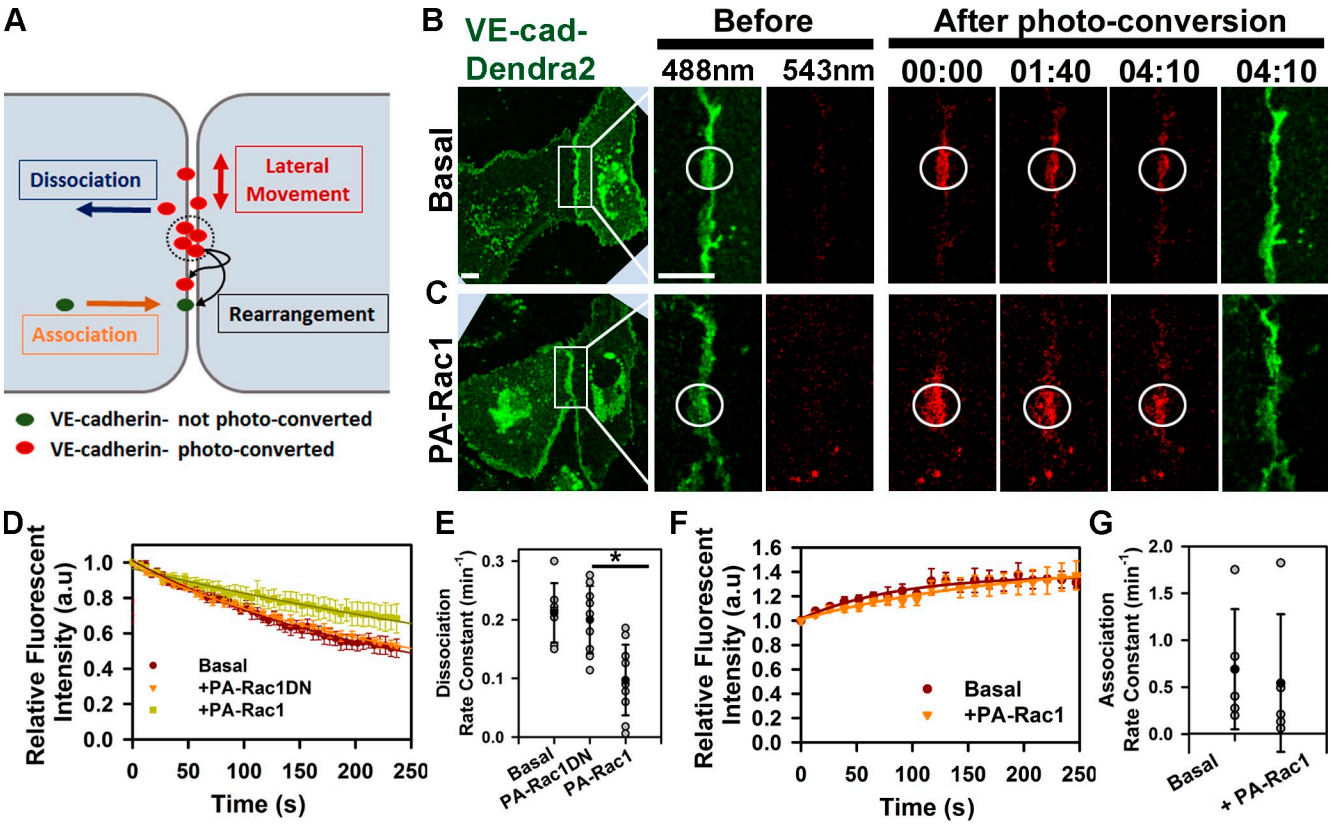

Figure 2. **Photoactivation of Rac1 at AJs decreases rate of VE-cadherin dissociation from AJs.** (A) Model representing VE-cadherin–Dendra2 kinetics at AJs. Photoconverted VE-cadherins within the irradiation zone (circles) undergo lateral movement and dissociation from AJs resulting in fluorescence intensity decay. They also undergo rearrangement of adhesive bonds with other photoconverted or newly recruited molecules. (B and C) Time-lapse images of VE-cadherin–Dendra2 (VE-cad-Dendra2) before (green) and after photoconversion (red, circles) at time 0 for basal (B) and PA-Rac1 activation (C). Time is given in minutes and seconds. Bars, 10 µm. (D) VE-cadherin dissociation rate is calculated from decay kinetics of Dendra2 after photoconversion; means ± SEM, $n = 7–10$. (E) Rate constants of VE-cadherin dissociation calculated from D for basal (0.21 ± 0.05 min^{-1}), PA-Rac1DN (0.2 ± 0.06 min^{-1}), and PA-Rac1 (0.1 ± 0.06 min^{-1}); means ± SD, $n = 7–10$; *, $P < 0.05$. (F) VE-cadherin association rate is determined from recovery kinetics of Dendra2 after photoconversion; means ± SEM, $n = 7–9$. (G) Rate constants of VE-cadherin association calculated from F for basal (0.69 ± 0.64 min^{-1}) and after PA-Rac1 activation (0.54 ± 0.73 min^{-1}); means ± SD, $n = 5$. a.u., arbitrary unit.

(Fig. 2, C–E) without an alteration in the association rate (Fig. 2, F and G; and Fig. S2, E and F). This shift in VE-cadherin kinetics after Rac1 activation was the result of spatiotemporal activity of PA-Rac1 because no changes in VE-cadherin kinetics were observed in the absence of photoactivation of PA-Rac1 (Fig. S2 C) or photoactivation of PA-Rac1DN (Fig. 2, C–E). Together, these results show that Rac1 stabilized VE-cadherin adhesion at mature AJs by decreasing the rate of VE-cadherin dissociation but without affecting the rate of association.

We next investigated the relationship between VE-cadherin kinetics at AJs as modulated by Rac1 activity and stability of trans-dimers. Structural analysis of the extracellular domain of VE-cadherin has shown that the strand-swap (trans) dimerization is the result of exchange between N-terminal β strands of opposing ectodomains (Brasch et al., 2011; Harrison et al., 2011) and is the primary event during cell–cell adhesion responsible for VE-cadherin homotypic interaction (Harrison et al., 2005; Zhang et al., 2009). The relationship between Rac1 activity and stability of VE-cadherin trans-dimers at mature AJs was initially assessed using an in silico model (Fig. 3, A–D). This model describes VE-cadherin adhesion (Fig. 3 A; Eqs. 1a and 1b) as an equilibrium between VE-cadherin monomers (reaction *a*) and trans-dimers (reaction *d*). After assuming symmetry in VE-cadherin distribution in mature cell–cell adhesions, the equilibrium between monomer and dimer was described by the equations

$$\frac{da}{dt} = j - k_a a - 2k_d^+ a^2 + 2k_d^- d \text{ and} \tag{1a}$$

$$\frac{dd}{dt} = k_d^+ a^2 - k_d^- d, \tag{1b}$$

in which j and $k_a a$ are the rates of VE-cadherin monomer–junction association and dissociation; k_d^+ and k_d^- are the "on" and "off" rate constants between the monomer and trans-dimer. The equilibrium relations between different states of VE-cadherin species were determined from Eqs. 1a and 1b.

The equations in the previous paragraph were solved using COPASI (Complex Pathway Simulator) software (Fig. 3, B–D). COPASI produced an optimal fit to our experimental data (i.e., monomer–junction association [j] and dissociation [k_a] rate constants [Fig. 2, E and G]), yielding a set of values for in silico on and off rates for trans-interaction (Fig. 3 D). Furthermore, the observed reduction in monomer–junction dissociation

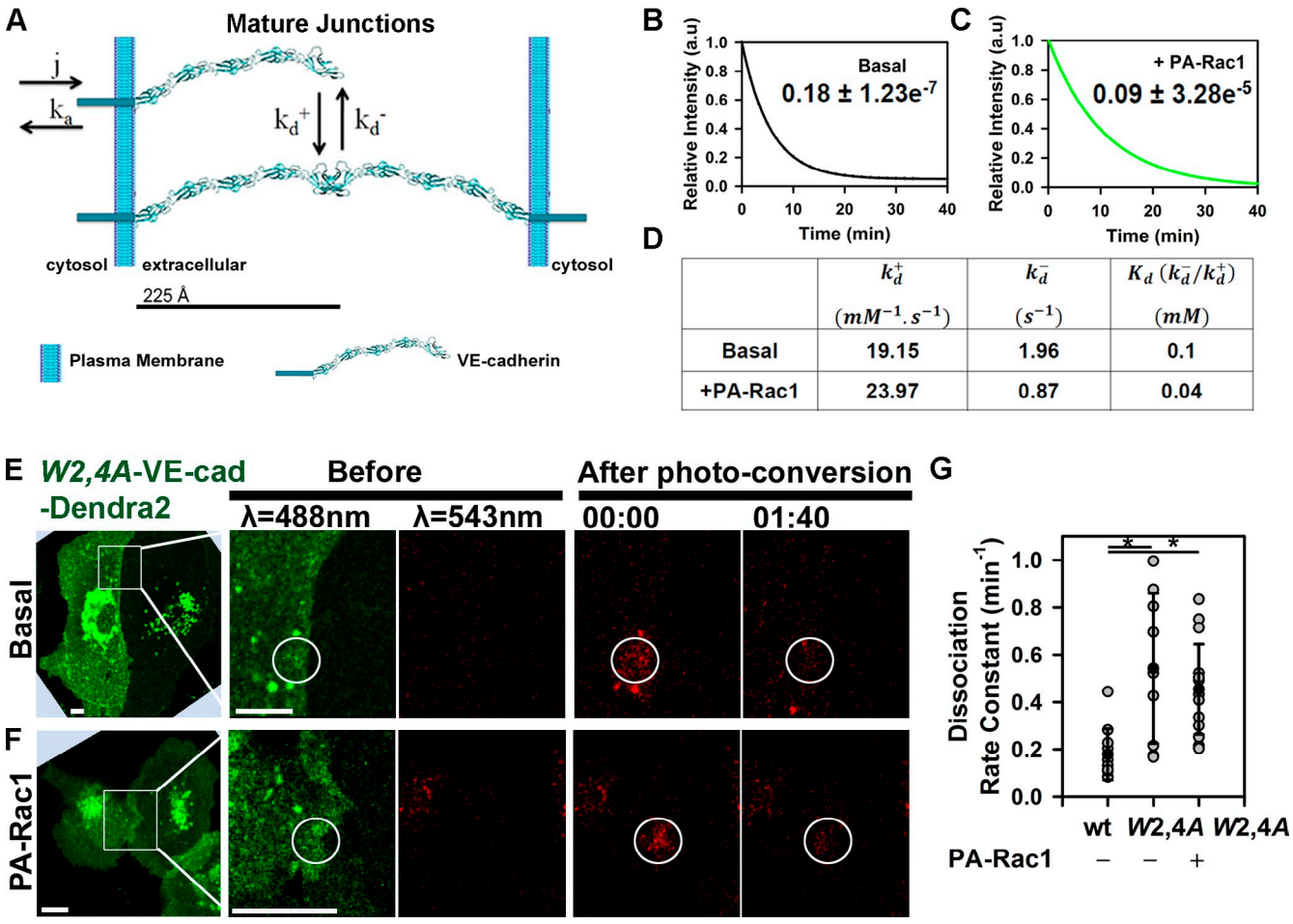

	k_d^+ $(mM^{-1}.s^{-1})$	k_d^- (s^{-1})	$K_d\ (k_d^-/k_d^+)$ (mM)
Basal	19.15	1.96	0.1
+PA-Rac1	23.97	0.87	0.04

Figure 3. **Relationship between VE-cadherin kinetics at AJs and stability of adhesive bonds.** (A) Mathematical model describing VE-cadherin monomer–junction association and dissociation rate constants (j and k_a) followed by reversible trans-dimerization characterized by k_d^+ and k_d^-. (B and C) COPASI-fitted experimental data from Fig. 2 (D and F) for basal (B) and after PA-Rac1 activation (C); dissociation rate constants are in minute^{-1} ± SEM. (D) Estimated values for k_d^+ and k_d^- described in A. (E and F) Time-lapse images of VE-cadherin–Dendra2 (VE-cad-Dendra2) *W2,4A* before and after photoconversion for basal (E) and PA-Rac1 activation (F) within the irradiation zone (circles). Time is in minutes and seconds. Bars, 10 µm. (G) Dissociation rate constant for wild type (0.18 ± 0.11 min^{-1}) and the *W2,4A* mutant without (0.54 ± 0.32 min^{-1}) and with PA-Rac1 activation (0.45 ± 0.19 min^{-1}); means ± SD, n = 9–15; *, P < 0.05. a.u., arbitrary unit.

rate constant after PA-Rac1 activation (k_a; Fig. 2 E) was accompanied by approximately twofold decrease in the off rate constant for trans-interaction (k_d^-; Fig. 3 D). The model based on the aforementioned assumptions predicted that Rac1 increases the affinity between trans-dimers and stabilizes VE-cadherin adhesion. To validate experimentally the in silico results, we determined the monomer–junction dissociation rate constant for VE-cadherin–Dendra2 bearing a substitution of two highly conserved tryptophan (W) residues at positions 2 and 4, the swapping elements required for trans-interaction (Brasch et al., 2011), to alanine (A). The W2A/W4A mutant displayed a threefold increase in the dissociation rate compared with the wild-type protein (Fig. 3, E and G). These data showed an inverse relationship between assembly of VE-cadherin adhesive bonds and dissociation rate, and they fully supported the in silico simulation in this paragraph. Importantly, activation of PA-Rac1 did not restore dynamics of the VE-cadherin mutant (Fig. 3, F and G), indicating the essential role of trans-dimerization in mediating Rac1-induced stabilization of VE-cadherin adhesions.

Rac1 activation occurred at sites of AJs experiencing the highest tension in response to fluid shear stress (Allen et al., 2011; Liu et al., 2013), suggesting that Rac1 functions by opposing the tension developed across VE-cadherin adhesion through counterbalancing RhoA activity (Fig. 4 A). To test this concept, we first used a Förster resonance energy transfer (FRET)–based RhoA biosensor (Pertz et al., 2006). Consistent with the antagonistic Rac1 and RhoA relationship (Yamada and Nelson, 2007), we observed spatial reduction of RhoA activity after photoactivation of PA-Rac1 but not of PI-Rac1 (Fig. 4, B–D). Furthermore, activation of PA-Rac1 significantly reduced phosphorylation of myosin-II light chain (MLCII) as compared with controls (Fig. 4, E–G). These findings suggest that Rac1 functioned at AJs by counterbalancing the RhoA-dependent tugging force across the VE-cadherin trans-dimers.

To measure directly actomyosin-mediated tension across VE-cadherin adhesion, we next used the tension sensor for VE-cadherin (VE-t; Fig. 4, H–J; Conway et al., 2013). Endothelial monolayers basally showed low FRET/CFP ratio (Fig. 4, H and I, inset 1), indicative of constitutive intracellular traction forces

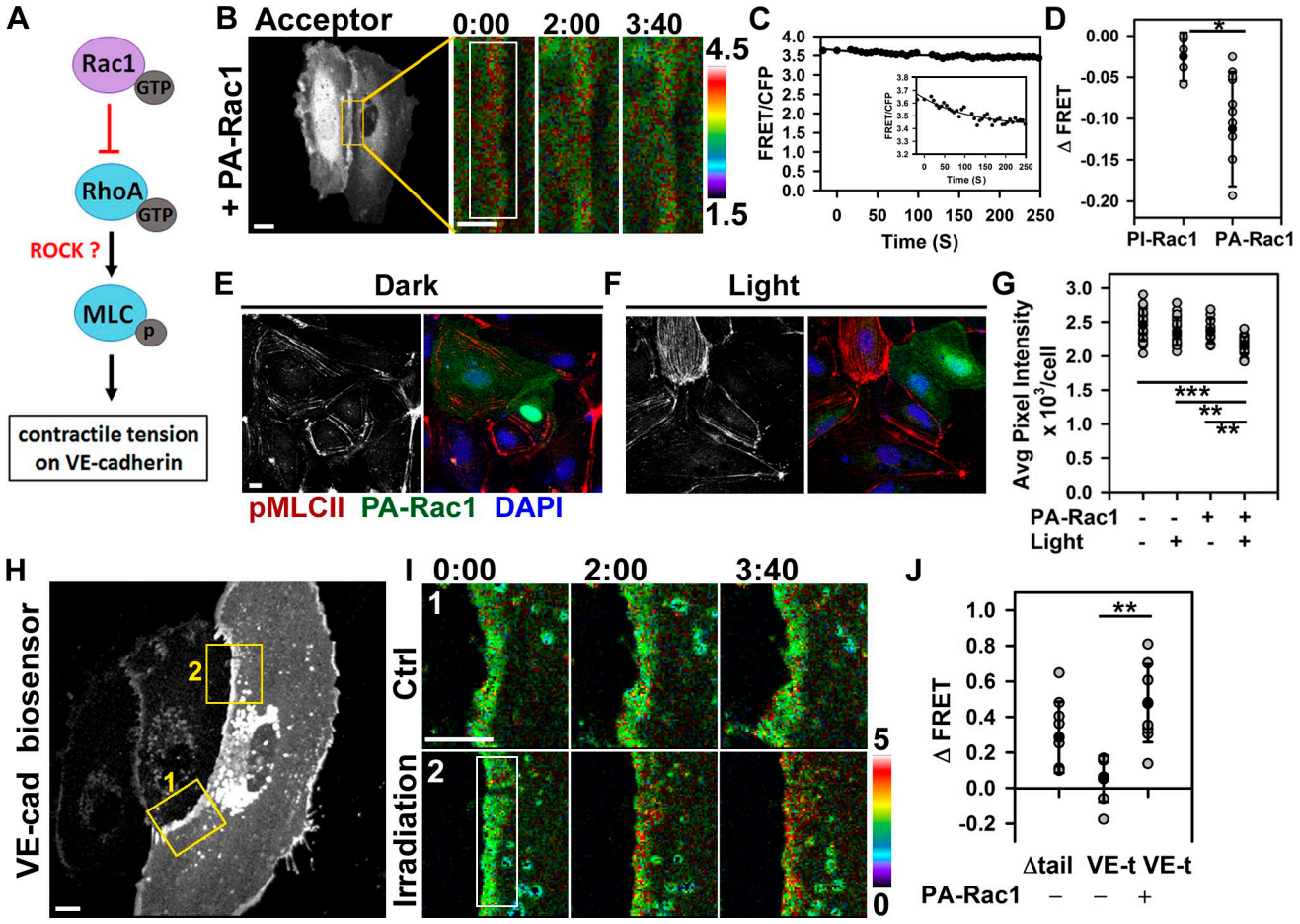

Figure 4. **Rac1 modulates actomyosin-mediated tension across VE-cadherin adhesion.** (A) Model of Rac1-mediated inhibition of RhoA–ROCK signaling and mechanical force across VE-cadherin adhesion. (B and C) Cells expressing RhoA biosensor and PA-Rac1. Changes in FRET/CFP ratio after PA-Rac1 activation at time 0 within the indicated region. Ratio images were scaled from 1.5 to 4.5 and color coded as indicated on the right. Representative tracer from reproducible dataset of $n = 10$. The inset within C is zoomed in on the graph to show the subtle drop in FRET signal. (D) Changes in RhoA activity after photoactivation of Pl-Rac1 (−0.03 ± 0.03) or PA-Rac1 (−0.11 ± 0.07); means ± SD, $n = 5$–10; *, $P < 0.05$. (E and F) Immunofluorescence staining for myosin light chain phosphorylation (pMLCII) without (dark; E) and with (light; F) Rac1 activation. (G) Quantification of p-MLCII in E and F; means ± SD, $n = 11$–21; **, $P < 0.005$; ***, $P < 0.0005$. (H) Cells expressing VE-cadherin (VE-cad) tension biosensor (VE-t) and PA-Rac1. Control (Ctrl; 1) and PA-Rac1 activation (irradiation; 2) zones are shown enlarged in I. (I) Spatial increase in FRET/CFP ratio was observed at the site of PA-Rac1 activation inside the rectangular region (2) but not the adjacent zone (1). Ratio images were scaled from 0 to 5. (J) Changes in FRET ratio for the tailless (tail) control and VE-t without or with PA-Rac1 activation; means ± SD, $n = 7$–10; **, $P < 0.005$. Times are given in minutes and seconds. Bars: (B [main image], E, H, and I) 10 µm; (B [insets]) 5 µm.

across VE-cadherin adhesions in the confluent endothelium. Photoactivation of Rac1, however, reduced basal tension of ∼2.4 nN/molecule to the level of the tailless control (Δtail), a probe that experiences no tension (Fig. 4, H and I, inset 2; Conway et al., 2013). Thus, transient activation of PA-Rac1 at AJs caused spatial relaxation and reduced the tension across VE-cadherin adhesions similar to that seen when applying fluid shear stress to confluent endothelial monolayers (Conway et al., 2013).

We determined whether transient inhibition of RhoA signaling downstream of Rac1 activation and the subsequent reduction in tension at AJs were sufficient to stabilize VE-cadherin transinteraction. Rho-associated protein kinase (ROCK) is a primary downstream effector of RhoA that inhibits myosin light chain phosphatase and phosphorylates MLCII, leading to actomyosin-dependent contractility (Riento and Ridley, 2003). To establish a causal relationship between RhoA–ROCK signaling and stability of VE-cadherin adhesions, we locally photo-released the caged ROCK inhibitor Rockout (caged Rockout [cRO]; Morckel et al., 2012). Release of cRO at AJs significantly reduced the tension across VE-cadherin adhesion (Fig. 5, A–C) and VE-cadherin dissociation rate from AJs (Fig. 5, D–F). cRO release thus also induced VE-cadherin accumulation at AJs (Fig. S3). Inhibition of MLCII activity with blebbistatin similarly reduced the VE-cadherin dissociation rate (Fig. 5, D–F). These data demonstrated that Rac1 activation through counteracting the RhoA–ROCK pathway reduced the tension applied to AJs that thereby stabilized VE-cadherin adhesion.

Cadherin-mediated adhesion provides the spatial cues for the recruitment of Rac1 at AJs through effectors phosphatidylinositide 3-kinase (Kovacs et al., 2002) and Tiam1 (T cell lymphoma invasion and metastasis-inducing protein 1; Lampugnani et al., 2002) and GTP loading through Vav2 (Liu et al., 2013). We observed that localized and transient Rac1 activation at AJs mediated VE-cadherin accumulation and stability of VE-cadherin

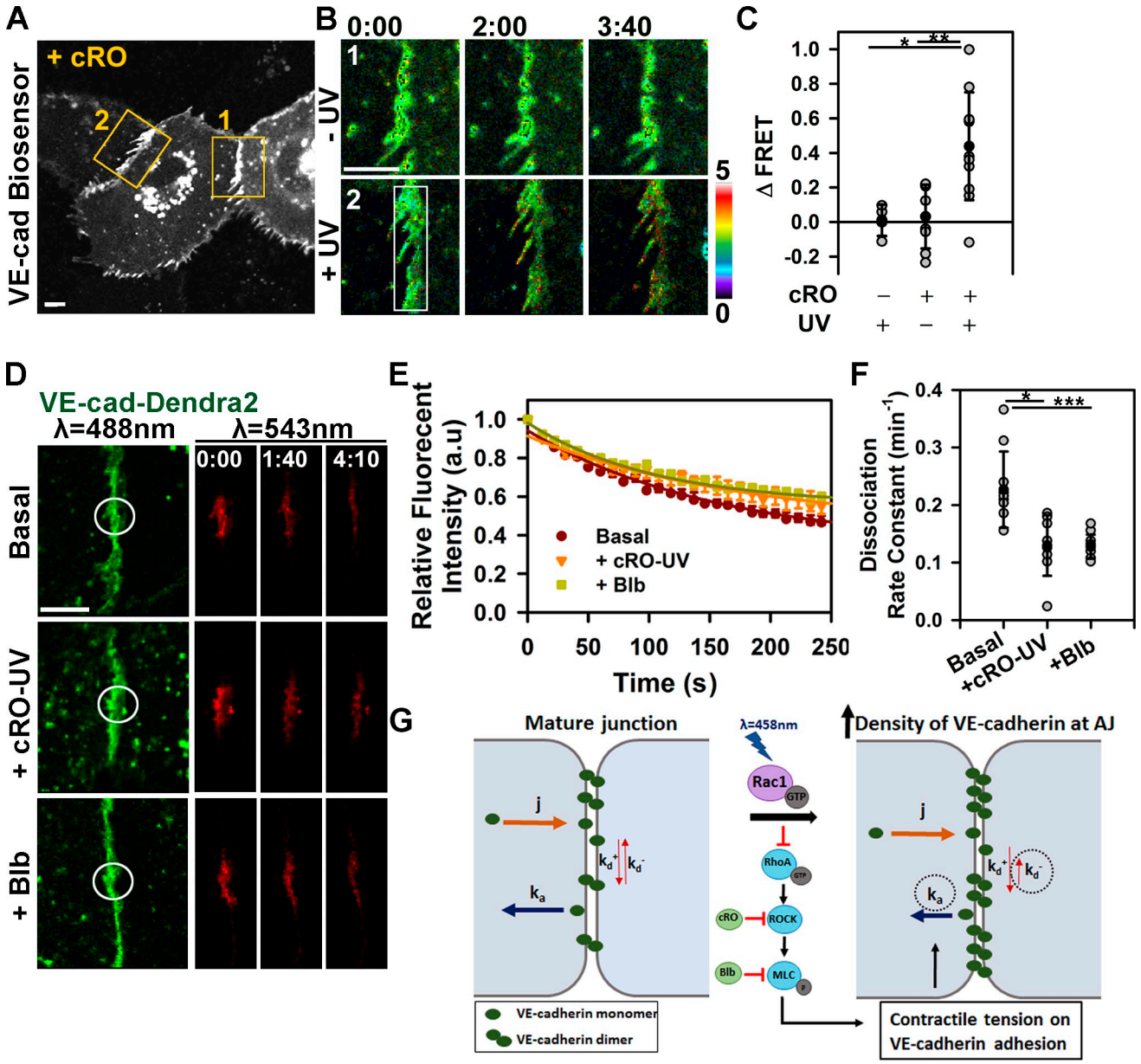

Figure 5. **Inhibition of actomyosin tension at AJs reduces the rate of VE-cadherin dissociation.** (A) Cells expressing VE-t and treated with cRO. FRET/CFP ratio was determined within the control (−UV; 1) and cRO uncaging (+UV; 2) zones, shown enlarged in B. VE-cad, VE-cadherin. (B) Spatial increase in FRET/CFP ratio after cRO uncaging within irradiation zone (2) and not the adjacent zone (1). Ratio images were scaled from 0 to 5. (C) Changes in FRET ratio for VE-t with and without cRO uncaging; means ± SD, n = 8–11; *, $P < 0.05$; **, $P < 0.005$. (D) Time-lapse images of VE-cadherin–Dendra2 before and after photoconversion within the irradiation zone (circles) in cells untreated (top; basal) or treated with cRO (middle) after uncaging or blebbistatin (bottom; +Blb). (E) VE-cadherin dissociation rate was calculated as in Fig. 2 D; means ± SEM, n = 6–12. a.u., arbitrary unit. (F) Rate constant of VE-cadherin dissociation calculated from E for basal (0.23 ± 0.07min^{-1}), cRO uncaging (0.13 ± 0.05 min^{-1}), and blebbistatin (0.13 ± 0.02 min^{-1}); means ± SD, n = 8–11 cells; *, $P < 0.05$; ***, $P < 0.0005$. (G) Working model of Rac1-mediated stabilization of VE-cadherin adhesion. Rac1 relieves actomyosin tension across the adhesion, by inhibiting RhoA–ROCK-mediated signaling, leading to increased affinity for VE-cadherin trans-interaction and decreased VE-cadherin dissociation from AJs. Times are given in minutes and seconds. Bars, 10 µm.

adhesive bonds by modulating actomyosin tension across VE-cadherin adhesions (Fig. 5 G). Interestingly, E-cadherin 1D to A mutation that stabilized trans-swapped dimers also assembled more stable adhesive clusters (Hong et al., 2013). The decrease in VE-cadherin dissociation rate mediated by PA-Rac1 was proportional to the increased VE-cadherin trans-interaction. Destabilization of this interaction with double W2A/W4A point mutations (Brasch et al., 2011) increased VE-cadherin dissociation rate and mitigated the effects of Rac1 activation on VE-cadherin dynamics. Together, our data indicate that Rac1 activity has a fundamental role in strengthening VE-cadherin adhesion at mature AJs experiencing mechanical tension.

Rac1 also induces formation of lamellipodia involved in annealing of nascent junctions and closure of inter-endothelial gaps after injury (Nola et al., 2011). However, Rac1 stabilization of VE-cadherin adhesive bonds in the present study occurred independently of formation of lamellipodia protrusions. Thus, the role of Rac1 in counterbalancing RhoA signaling at the level

of mature AJs and stabilizing trans-dimers (Fig. 5 G) is distinct from the role of Rac1 in establishing endothelial junctional barrier through lamellipodia formation. The mechanism of Rac1 inhibition of RhoA activity at AJs is unknown. We previously showed that p190RhoGAP-A inhibited RhoA activity at AJs and that the GTPase-activating protein (GAP) activity was regulated by tyrosine nitration at Y^{1105} (Siddiqui et al., 2011). In epithelial cells, P190RhoGAP-B appears to be the GAP responsible for controlling RhoA activity (Ponik et al., 2013), suggesting that the function of GAPs in regulation RhoA activity at AJs may be cell specific. Importantly, both GAPs required interaction with p120-catenin to inhibit RhoA and protect against permeability increase (Ponik et al., 2013; Zebda et al., 2013). Rac1 and its upstream effectors Tiam1 and Vav2 may be required for localization of P190RhoGAP to the junctions (Wildenberg et al., 2006; Birukova et al., 2011).

In conclusion, we describe here a novel mechanism by which Rac1 relieves myosin-dependent tension across VE-cadherin junctions and stabilizes VE-cadherin trans-interaction at mature AJs of confluent endothelial cells. This tug-of-war between Rac1 and RhoA ensures prompt restoration of barrier function of AJs after immune and inflammatory insults to regulate tissue fluid balance.

Materials and methods

Plasmids and adenovirus

The human VE-cadherin–GFP adenovirus (pAdRSV4, the dL327 backbone, cytomegalovirus [CMV] promoter; Shaw et al., 2001) was a gift from F. Luscinskas (Brigham and Women's Hospital, Boston, MA) and S.K. Shaw (Brown University, Providence, RI). VE-cadherin–Dendra2 (pCDNA3 and CMV promoter) was generated by PCR-based strategy and subcloning VE-cadherin and Dendra2 (a gift from S. Troyanovsky, Northwestern University, Chicago, IL; Hong et al., 2010), into the pCDNA3 vector (Life Technologies) at restriction sites 5′-KpnI and 3′-EcoRI for VE-cadherin and 5′-EcoRI and 3′-XhoI sites for Dendra2. Mutation of tryptophan residues at positions 2 and 4 to alanine (W2A/W4A) on VE-cadherin was generated using a site-directed mutagenesis kit (QuikChange; Agilent Technologies). VE-cadherin tension (VE-t) and tailless (tail) control FRET-based biosensors were used (pLPCX and CMV promoter; Conway et al., 2013). mCherry-PA-Rac1, mCerrulean-PA-Rac1, mCherry-PA-Rac1-T17N (PA-Rac1DN), mVenus-PA-Rac1-T17N (PA-Rac1DN), and mCherry-PA-Rac1-C450A (PI-Rac1; pTriEx, a hybrid promoter composed of the CMV enhancer fused to the chicken β-actin promoter; Wu et al., 2009) and the FRET-based RhoA biosensor (pTriEx, a hybrid promoter; Pertz et al., 2006) were gifts from K. Hahn (University of North Carolina School of Medicine, Chapel Hill, NC). For CFP-PA-Rac1DN, CFP was amplified using pECFP-C1 (BD) as a DNA template and subcloned into pTriEx-mVenus-PA-Rac1-T17N using 5′-NcoI and 3′-BamHI restriction sites.

Synthesis of cRO

cRO was synthesized according to Morckel et al. (2012) with some modifications. In brief, starting material NPOM-Cl (6-nitropiperonyloxymethyl-chloride) was first prepared according to Lusic and Deiters (2006). A mixture of 10.0 mg ROCK inhibitor III (Rockout) and 1 ml dimethylformamide was stirred on ice for 5 min. 1.4 mg sodium hydride (0.058 mmol) was added to the mixture, stirred on ice for an additional hour, and frozen solid using a dry ice/acetone bath. Next, 0.3 ml dimethylformamide containing 20.5 mg NPOM-Cl (0.079 mmol) was added to the frozen mixture and stirred at room temperature for 12 h before quenching with 1 ml saturated sodium bicarbonate. The solution was extracted with 10 ml ethyl acetate, dried over sodium sulfate, and concentrated in vacuo. The crude product was purified via silica column chromatography. A mobile phase of 7:3 hexanes/ethyl acetate (vol/vol) removed byproducts and unreacted material, and the product was eluded with a mobile phase of 100% ethyl acetate to yield 5.2 mg (24% yield) of pure cRO as yellow flakes. Purity was assessed via ^{1}H–nuclear magnetic resonance (NMR) spectroscopy. ^{1}H-NMR spectra were acquired on a 360 MHz NMR spectrometer (AVANCE; Bruker) and were obtained in $CDCl_3$ using 0.01% tetramethylsilane as an internal standard. Electrospray mass spectra (positive ion mode) were obtained on a mass spectrometer (IT-TOF [ion trap time-of-flight]; Shimadzu).

Cell culture, transfection, and treatment

Human dermal microvascular endothelial cells (HMECs; Ades et al., 1992) were grown in MCDB 131 medium (Gibco) supplemented with 10% FBS, 0.003 mg/ml human EGF, 0.001 mg/ml hydrocortisone, and L-glutamine. Primary human pulmonary arterial endothelial cells were grown in EBM-2 culture medium (Lonza) supplemented with 15% FBS and EGM-2 bullet kit (Lonza) and were used at passages 2–6. All cell lines were maintained at 37°C and 5% CO_2.

Endothelial cells were plated on glass-bottom coverslips coated with 0.2% gelatin and transfected at 70–80% confluency using X-tremeGENE HP DNA transfection reagent according to manufacturer's protocol (Roche). For adenoviral infection, endothelial cells were exposed to the adenoviral particles overnight and were used for live-cell imaging at 24–72 h after infection. The procedure was handled according to National Institutes of Health safety guidelines for materials containing BSL-2 organisms. Cells were treated with 20 µM cRO or 10 µM blebbistatin (Toronto Research Chemicals) for 10 min before experiments.

Immunofluorescence staining and analysis of MLCII phosphorylation

Cells expressing mCerulean-PA-Rac1 (Fig. 4, E and F, shown in green) were kept in dark or exposed to white light for 10 min. Cells were fixed with 4% paraformaldehyde (Electron Microscopy Sciences) and permeabilized with 0.2% Triton X-100. Nonspecific sites were blocked with 4% BSA. Samples were stained for phosphorylated MLCII using the rabbit polyclonal phospho-Thr18/Ser19–specific antibody (3674; Cell Signaling Technology) and TRITC-conjugated donkey anti–rabbit antibody (Jackson ImmunoResearch Laboratories, Inc.). In addition, a mouse monoclonal GFP antibody (A11120; Life Technologies) and FITC-conjugated anti–mouse antibody (Jackson ImmunoResearch Laboratories, Inc.) were used to stain for mCerulean-PA-Rac1; however, the antibody was found to be nonspecific (staining not depicted in Fig. 4, E and F). Samples were mounted in ProLong Gold reagent (Molecular Probes). Z-stack images were obtained at room temperature using a confocal microscope (LSM 510 Meta; Carl Zeiss) equipped with a 63×, 1.2 NA water immersion objective lenses and Ar ion and dual HeNe lasers and driven by LSM software (Carl Zeiss). Image handling and analysis were performed using MetaMorph software (Molecular Devices), and images were prepared for illustration in Photoshop (Adobe). Cell staining was used to define cell boundaries caused by nonspecificity of the GFP antibody. Transfected cells were chosen using the CFP channel (λ = 458 nm). In these cells, the CFP fluorescence was used to define the cell boundary between dark and light conditions. Relative phosphorylation of MLCII was expressed as mean pixel intensity above background noise. Z-stack images were projected onto a single image. An image with high signal was used to define the threshold for mean pixel intensities and to remove background noise. The threshold value excluded almost all background noise and stress fibers and included only the bright signal from the cortical actin. The same value for the mean pixel intensities was used to threshold all images, thus keeping analysis consistent. The values for mean pixel intensity of threshold images were measured for each cell.

Live-cell imaging

In all experiments, endothelial cells were imaged in phenol red–free EBM-2 media supplemented with 5% FBS at 37°C using the stage heater (Tempcontrol 37; Carl Zeiss). Time-lapse images were acquired using confocal microscope (LSM 710; Carl Zeiss) equipped with a 63×, 1.4 NA oil immersion objective lenses and Ar ion and dual HeNe lasers and driven by LSM software. Image handling and analysis were performed using MetaMorph software and prepared for illustration in Photoshop.

To determine the effect of Rac1 on VE-cadherin density at AJs, cells coexpressing VE-cadherin–GFP and PA-Rac1-mCherry were imaged with λ = 488-nm and λ = 543-nm laser, respectively. Photoactivation was achieved with λ = 458-nm laser beam at 70% power for ∼10 s at a selected region, and images in green channel were acquired every 5 s. For studying VE-cadherin kinetics, cells coexpressing VE-cadherin–Dendra2 and PA-Rac1-CFP were imaged with λ = 488 nm and λ = 543 nm for green and red states of Dendra2, respectively, and λ = 458 nm for CFP. Dendra2 was photoconverted with λ = 405-nm laser at 8–12% power. Images in green and red channels were simultaneously acquired every 5 s. For FRET emission ratio imaging, 12-bit CFP (λ = 458 nm; band pass 500/20 nm), FRET (λ = 458 nm; long pass 530 nm), and YFP (λ = 514 nm; long pass 530 nm) were acquired.

Image processing

All images were corrected for photobleaching using a modified version of MATLAB software (MathWorks; Hodgson et al., 2006). A photobleaching coefficient was determined from decay kinetics of fluorescent intensity outside of Rac1 photoactivation zone. Each image of time-lapse sequence was corrected for photobleaching, exported to 16-bit format using the LSM program, and analyzed using MetaMorph software.

VE-cadherin–GFP density at AJs was expressed as mean fluorescent intensity of GFP at AJs (above intracellular background) within the photoactivation zone. The increase in VE-cadherin fluorescence after activation of PA-Rac1 or uncaging of cRO above the initial basal values was expressed as relative fluorescent amplitude. The rate constants were calculated by fitting data to a single exponential rise curve.

VE-cadherin–GFP adhesion area was determined by selecting pixels of high intensity values (i.e., VE-cadherin adhesion) using a threshold mapping function in MetaMorph software. The percentage of threshold area within the photoactivation zone was measured before and at 5 min of PA-Rac1 photoactivation.

VE-cadherin kinetics at AJs was assessed with VE-cadherin–Dendra2. The changes in mean fluorescent intensities at 488- and 543-nm maximum emission spectra were measured inside the photoconversion zone. The rate constants for VE-cadherin dissociation (at 543 nm) and association (at 488 nm) were calculated from decay and recovery kinetics, respectively, after VE-cadherin–Dendra2 photoconversion. The rate of VE-cadherin–Dendra2 lateral movement within the cell–cell junction was determined from the rate of fluorescence lateral movement at λ = 543 nm outside of the photoconversion region using kymograph analyses.

For FRET analysis, YFP and CFP channels were corrected for photobleaching. Photobleaching coefficient obtained for YFP was used to correct both YFP and FRET images. The CFP image was corrected using the CFP photobleaching coefficient. The YFP image was used to create a binary mask with a value of 0 outside the cell and a value of 1 inside the cell. To generate a ratio image, the FRET image was first multiplied by a binary mask image and then divided by the CFP image. The ratio images were rescaled to the lower value, and a linear pseudocolor table was applied to generate the color-coded image map. For quantification of FRET data shown in Fig. 4 (C and D), a region that included only the thick area (i.e., junctions or membrane overlap) between the two cells within the photoactivation zone was used. The integrated intensity for FRET and CFP within this region was measured for each frame, and numbers were divided to get the FRET/CFP ratio for each frame. Ratios were plotted over time and fitted to an exponential decay. The change in ratio from time 0 to the time at which the curve reaches a plateau was determined. Importantly, quantifications in Fig. 4 (C and D) were based on the integrated intensities and not from the FRET/CFP ratio images (as shown in Fig. 4 B). The relative activity of RhoA and tension were expressed as mean pixel intensity of FRET/CFP ratio within the irradiation zone at AJs. The changes in RhoA activity or tension across VE-cadherin adhesion were determined before and after PA-Rac1 activation or cRO photo-uncaging.

Computational modeling and parameter estimation

COPASI software was used to fit our experimental data as well as to perform parameter estimation. We assumed that all VE-cadherin–Dendra2 molecules emitted green fluorescence before photoconversion and obeyed rules established by Eqs. 1a and 1b.

The equilibrium relations between different states of VE-cadherin species were determined from Eqs. 1a and 1b as follows:

$$a = \frac{j}{k_a} \text{ and} \tag{2a}$$

$$d = \frac{a^2}{K_d}, \tag{2b}$$

in which $K_d = k_d^- / k_d^+$ describes the affinity between two opposing VE-cadherin molecules forming a trans-dimer.

However, only a fraction of these molecules (at equal probability) emitted a red fluorescence after photoconversion. It was experimentally estimated that 70% of VE-cadherin–Dendra2 molecules underwent a photoconversion. These photoconverted molecules were distinguished from the others using an asterisk symbol. We assumed that VE-cadherin molecules existing either as a monomer or as a part of the dimer had an equal probability for photoconversion and were assigned with number of asterisks equal to the number of photoconverted molecules within the complex. For example, the monomer had only one asterisk, and the dimer could have either one or two asterisks. Therefore, the governing reactions shown below (based on Fig. 3 A) can be described as VE-cadherin monomer–junction associations and dissociations with asterisks depicting the number of photoconverted molecules (ranging from 0 to 1; first and second reactions) and reversible dimerization of two monomers with asterisks depicting the number of photoconverted molecules (ranging from 0 to 2; third through fifth reactions).

$$\xrightarrow{j} a \xrightarrow{k_a} \varnothing,$$

$$a_* \xrightarrow{k_a} \varnothing,$$

$$2a \underset{k_d^-}{\overset{k_d^+}{\rightleftharpoons}} d,$$

$$a_* + a \underset{k_d^-}{\overset{k_d^+}{\rightleftharpoons}} d_*, \text{ and}$$

$$2a_* \underset{k_d^-}{\overset{k_d^+}{\rightleftharpoons}} d_{**}.$$

Subsequent to photobleaching, the governing mass balance equations are

$$\frac{da}{dt} = j - k_a a - 2k_d^+ a^2 + 2k_d^- d - k_d^+ a a_* + k_d^- d_*, \tag{3a}$$

$$\frac{da_*}{dt} = -k_a a_* - k_d^+ a a_* + k_d^- d_* - 2k_d^+ a_*^2 + 2k_d^- d_{**}, \tag{3b}$$

$$\frac{dd}{dt} = k_d^+ a^2 - k_d^- d, \tag{3c}$$

$$\frac{dd_*}{dt} = k_d^+ a a_* - k_d^- d_*, \text{ and} \tag{3d}$$

$$\frac{dd_{**}}{dt} = k_d^+ a_*^2 - k_d^- d_{**}. \tag{3e}$$

The equilibrium relations presented in Eqs. 2a and 2b are shown with γ, the fraction of photoconverted molecules (ranging from 0 to 1) at time 0 in Eqs. 4a–4e. a_t is the total amount of a (which is 1). Introduction of γ allows us to derive the initial equilibrium relations for the model that includes photoconverted and nonphotoconverted VE-cadherin species, under the assumption that the monomers are photoconverted independently of one another even if they form a trans-dimer.

$$a = (1-\gamma) a_t, \tag{4a}$$

$$a_* = \gamma a_t, \tag{4b}$$

$$d = \frac{a^2}{K_d} = \frac{(1-\gamma)^2 a_t}{K_d}, \tag{4c}$$

$$d_* = 2\left(\frac{a a_*}{K_d}\right) = \frac{2\gamma(1-\gamma)a_t}{K_d}, \text{ and} \tag{4d}$$

$$d_{**} = \frac{a_*^2}{K_d} = \frac{\gamma^2 a_t}{K_d}. \tag{4e}$$

These reactions and the steady-state values were given to COPASI. Values for j and k_a were based on experimental measurements (Fig. 2, E and G). The value for j was fixed at 0.01 s^{-1}, and the value for k_a was fixed at 0.003 s^{-1} for basal condition and 0.0016 s^{-1} after PA-Rac1 photoactivation (obtained from the VE-cadherin–Dendra2 experiment). For k_d^-, a lower boundary of 1 s^{-1} and a higher boundary of 2 s^{-1} were given, and for k_d^+, a lower boundary of 1 mM^{-1} s^{-1} and a higher boundary of 100 mM^{-1} s^{-1} were given to COPASI based on previous publications (Baumgartner et al., 2000; Häussinger et al., 2004). A constraint was added for the binding affinity (K_d) with lower boundary of 0.01 mM and upper boundary of 1 mM, also based on previous publications (Baumgartner et al., 2000; Häussinger et al., 2004; Katsamba et al., 2009). A set of values for basal k_d^+ and k_d^- parameters was estimated by fitting the experimental data (Fig. 2 D, Basal) to the total concentration equation:

$$s_* = a_* + d_* + 2d_{**}.$$

The equation establishes the relation between the photobleach signal (s_*) and the forms of photobleached trans-dimers. This process was repeated to fit experimental data (Fig. 2 D, PA-Rac1) and to estimate parameters after PA-Rac1 photoactivation. In this scenario, the constraint for k_d^- was removed to assess the effect of Rac1.

Online supplemental material

Fig. S1 shows the effect of PA-Rac1 activation on VE-cadherin density in HMECs as well as the effect of Rac1 on adhesion area. Fig. S2 describes the role of Rac1 on VE-cadherin kinetics, specifically on VE-cadherin recruitment to the junction. Fig. S3 provides a relationship between localized inhibition of ROCK and VE-cadherin density at AJs. Online supplemental material is available at http://www.jcb.org/cgi/content/full/jcb.201409108/DC1. Additional data are available in the JCB DataViewer at http://dx.doi.org/10.1083/jcb.201409108.dv.

We thank the University of Illinois at Chicago Core Imaging Facility, Drs. T. Sharma and F. Huang for technical assistance, the Cold Spring Harbor Laboratory Computational Cell Biology Course, and Dr. G.D. Smith (The College of William and Mary, Williamsburg, VA) for constructive suggestions regarding the modeling.

This work was supported by American Heart Association grant 13PRE14670018 to N. Daneshjou, Netherlands Heart Foundation grant 2011T072 to G.P. van Nieuw Amerongen, and National Institutes of Health grants R01 HL103922 to Y.A. Komarova and T32 HL007829-18, P01 HL60678, and RO1 HL45638 to A.B. Malik. The work presented in this paper fulfills in part the PhD degree requirement for N. Daneshjou.

The authors declare no competing financial interests.

Submitted: 23 September 2014
Accepted: 1 December 2014

References

Ades, E.W., F.J. Candal, R.A. Swerlick, V.G. George, S. Summers, D.C. Bosse, and T.J. Lawley. 1992. HMEC-1: establishment of an immortalized human microvascular endothelial cell line. *J. Invest. Dermatol.* 99:683–690. http://dx.doi.org/10.1111/1523-1747.ep12613748

Allen, R.J., I.D. Bogle, and A.J. Ridley. 2011. A model of localised Rac1 activation in endothelial cells due to fluid flow. *J. Theor. Biol.* 280:34–42. http://dx.doi.org/10.1016/j.jtbi.2011.03.021

Baumgartner, W., P. Hinterdorfer, W. Ness, A. Raab, D. Vestweber, H. Schindler, and D. Drenckhahn. 2000. Cadherin interaction probed by atomic force microscopy. *Proc. Natl. Acad. Sci. USA*. 97:4005–4010. http://dx.doi.org/10.1073/pnas.070052697

Baumgartner, W., G.J. Schütz, J. Wiegand, N. Golenhofen, and D. Drenckhahn. 2003. Cadherin function probed by laser tweezer and single molecule fluorescence in vascular endothelial cells. *J. Cell Sci.* 116:1001–1011. http://dx.doi.org/10.1242/jcs.00322

Birukova, A.A., N. Zebda, I. Cokic, P. Fu, T. Wu, O. Dubrovskyi, and K.G. Birukov. 2011. p190RhoGAP mediates protective effects of oxidized phospholipids in the models of ventilator-induced lung injury. *Exp. Cell Res.* 317:859–872. http://dx.doi.org/10.1016/j.yexcr.2010.11.011

Brasch, J., O.J. Harrison, G. Ahlsen, S.M. Carnally, R.M. Henderson, B. Honig, and L. Shapiro. 2011. Structure and binding mechanism of vascular endothelial cadherin: a divergent classical cadherin. *J. Mol. Biol.* 408:57–73. http://dx.doi.org/10.1016/j.jmb.2011.01.031

Cain, R.J., B. Vanhaesebroeck, and A.J. Ridley. 2010. The PI3K p110α isoform regulates endothelial adherens junctions via Pyk2 and Rac1. *J. Cell Biol.* 188:863–876. http://dx.doi.org/10.1083/jcb.200907135

Chudakov, D.M., S. Lukyanov, and K.A. Lukyanov. 2007. Tracking intracellular protein movements using photoswitchable fluorescent proteins PS-CFP2 and Dendra2. *Nat. Protoc.* 2:2024–2032. http://dx.doi.org/10.1038/nprot.2007.291

Conway, D.E., M.T. Breckenridge, E. Hinde, E. Gratton, C.S. Chen, and M.A. Schwartz. 2013. Fluid shear stress on endothelial cells modulates mechanical tension across VE-cadherin and PECAM-1. *Curr. Biol.* 23:1024–1030. http://dx.doi.org/10.1016/j.cub.2013.04.049

de Beco, S., C. Gueudry, F. Amblard, and S. Coscoy. 2009. Endocytosis is required for E-cadherin redistribution at mature adherens junctions. *Proc. Natl. Acad. Sci. USA*. 106:7010–7015. http://dx.doi.org/10.1073/pnas.0811253106

Ehrlich, J.S., M.D. Hansen, and W.J. Nelson. 2002. Spatio-temporal regulation of Rac1 localization and lamellipodia dynamics during epithelial cell-cell adhesion. *Dev. Cell*. 3:259–270. http://dx.doi.org/10.1016/S1534-5807(02)00216-2

Eriksson, A., R. Cao, J. Roy, K. Tritsaris, C. Wahlestedt, S. Dissing, J. Thyberg, and Y. Cao. 2003. Small GTP-binding protein Rac is an essential mediator of vascular endothelial growth factor-induced endothelial fenestrations and vascular permeability. *Circulation*. 107:1532–1538. http://dx.doi.org/10.1161/01.CIR.0000055324.34758.32

Giannotta, M., M. Trani, and E. Dejana. 2013. VE-cadherin and endothelial adherens junctions: active guardians of vascular integrity. *Dev. Cell*. 26:441–454. http://dx.doi.org/10.1016/j.devcel.2013.08.020

Harrison, O.J., E.M. Corps, T. Berge, and P.J. Kilshaw. 2005. The mechanism of cell adhesion by classical cadherins: the role of domain 1. *J. Cell Sci.* 118:711–721. http://dx.doi.org/10.1242/jcs.01665

Harrison, O.J., X. Jin, S. Hong, F. Bahna, G. Ahlsen, J. Brasch, Y. Wu, J. Vendome, K. Felsovalyi, C.M. Hampton, et al. 2011. The extracellular architecture of adherens junctions revealed by crystal structures of type I cadherins. *Structure*. 19:244–256. http://dx.doi.org/10.1016/j.str.2010.11.016

Häussinger, D., T. Ahrens, T. Aberle, J. Engel, J. Stetefeld, and S. Grzesiek. 2004. Proteolytic E-cadherin activation followed by solution NMR and X-ray crystallography. *EMBO J.* 23:1699–1708. http://dx.doi.org/10.1038/sj.emboj.7600192

Hodgson, L., P. Nalbant, F. Shen, and K. Hahn. 2006. Imaging and photobleach correction of Mero-CBD, sensor of endogenous Cdc42 activation. *Methods Enzymol.* 406:140–156. http://dx.doi.org/10.1016/S0076-6879(06)06012-5

Hong, S., R.B. Troyanovsky, and S.M. Troyanovsky. 2010. Spontaneous assembly and active disassembly balance adherens junction homeostasis. *Proc. Natl. Acad. Sci. USA*. 107:3528–3533. http://dx.doi.org/10.1073/pnas.0911027107

Hong, S., R.B. Troyanovsky, and S.M. Troyanovsky. 2011. Cadherin exits the junction by switching its adhesive bond. *J. Cell Biol.* 192:1073–1083. http://dx.doi.org/10.1083/jcb.201006113

Hong, S., R.B. Troyanovsky, and S.M. Troyanovsky. 2013. Binding to F-actin guides cadherin cluster assembly, stability, and movement. *J. Cell Biol.* 201:131–143. http://dx.doi.org/10.1083/jcb.201211054

Katsamba, P., K. Carroll, G. Ahlsen, F. Bahna, J. Vendome, S. Posy, M. Rajebhosale, S. Price, T.M. Jessell, A. Ben-Shaul, et al. 2009. Linking molecular affinity and cellular specificity in cadherin-mediated adhesion. *Proc. Natl. Acad. Sci. USA*. 106:11594–11599. http://dx.doi.org/10.1073/pnas.0905349106

Komarova, Y., and A.B. Malik. 2010. Regulation of endothelial permeability via paracellular and transcellular transport pathways. *Annu. Rev. Physiol.* 72:463–493. http://dx.doi.org/10.1146/annurev-physiol-021909-135833

Kovacs, E.M., R.G. Ali, A.J. McCormack, and A.S. Yap. 2002. E-cadherin homophilic ligation directly signals through Rac and phosphatidylinositol 3-kinase to regulate adhesive contacts. *J. Biol. Chem.* 277:6708–6718. http://dx.doi.org/10.1074/jbc.M109640200

Lampugnani, M.G., A. Zanetti, F. Breviario, G. Balconi, F. Orsenigo, M. Corada, R. Spagnuolo, M. Betson, V. Braga, and E. Dejana. 2002. VE-cadherin regulates endothelial actin activating Rac and increasing membrane association of Tiam. *Mol. Biol. Cell*. 13:1175–1189. http://dx.doi.org/10.1091/mbc.01-07-0368

Lee, M.J., S. Thangada, K.P. Claffey, N. Ancellin, C.H. Liu, M. Kluk, M. Volpi, R.I. Sha'afi, and T. Hla. 1999. Vascular endothelial cell adherens junction assembly and morphogenesis induced by sphingosine-1-phosphate. *Cell*. 99:301–312. http://dx.doi.org/10.1016/S0092-8674(00)81661-X

Liu, Y., C. Collins, W.B. Kiosses, A.M. Murray, M. Joshi, T.R. Shepherd, E.J. Fuentes, and E. Tzima. 2013. A novel pathway spatiotemporally activates Rac1 and redox signaling in response to fluid shear stress. *J. Cell Biol.* 201:863–873. http://dx.doi.org/10.1083/jcb.201207115

Lusic, H., and A. Deiters. 2006. A new photocaging group for aromatic N-heterocycles. *Synthesis*. 13:2147–2150.

Mehta, D., M. Konstantoulaki, G.U. Ahmmed, and A.B. Malik. 2005. Sphingosine 1-phosphate-induced mobilization of intracellular Ca2+ mediates rac activation and adherens junction assembly in endothelial cells. *J. Biol. Chem.* 280:17320–17328. http://dx.doi.org/10.1074/jbc.M411674200

Monaghan-Benson, E., and K. Burridge. 2009. The regulation of vascular endothelial growth factor-induced microvascular permeability requires Rac and reactive oxygen species. *J. Biol. Chem.* 284:25602–25611. http://dx.doi.org/10.1074/jbc.M109.009894

Morckel, A.R., H. Lusic, L. Farzana, J.A. Yoder, A. Deiters, and N.M. Nascone-Yoder. 2012. A photoactivatable small-molecule inhibitor for light-controlled spatiotemporal regulation of Rho kinase in live embryos. *Development*. 139:437–442. http://dx.doi.org/10.1242/dev.072165

Naikawadi, R.P., N. Cheng, S.M. Vogel, F. Qian, D. Wu, A.B. Malik, and R.D. Ye. 2012. A critical role for phosphatidylinositol (3,4,5)-trisphosphate-dependent Rac exchanger 1 in endothelial junction disruption and vascular hyperpermeability. *Circ. Res.* 111:1517–1527. http://dx.doi.org/10.1161/CIRCRESAHA.112.273078

Nola, S., R. Daigaku, K. Smolarczyk, M. Carstens, B. Martin-Martin, G. Longmore, M. Bailly, and V.M. Braga. 2011. Ajuba is required for Rac activation and maintenance of E-cadherin adhesion. *J. Cell Biol.* 195: 855–871. http://dx.doi.org/10.1083/jcb.201107162

Noren, N.K., C.M. Niessen, B.M. Gumbiner, and K. Burridge. 2001. Cadherin engagement regulates Rho family GTPases. *J. Biol. Chem.* 276:33305–33308. http://dx.doi.org/10.1074/jbc.C100306200

Pertz, O., L. Hodgson, R.L. Klemke, and K.M. Hahn. 2006. Spatiotemporal dynamics of RhoA activity in migrating cells. *Nature*. 440:1069–1072. http://dx.doi.org/10.1038/nature04665

Ponik, S.M., S.M. Trier, M.A. Wozniak, K.W. Eliceiri, and P.J. Keely. 2013. RhoA is down-regulated at cell-cell contacts via p190RhoGAP-B in response to tensional homeostasis. *Mol. Biol. Cell*. 24:1688–1699: S1–S3. http://dx.doi.org/10.1091/mbc.E12-05-0386

Riento, K., and A.J. Ridley. 2003. Rocks: multifunctional kinases in cell behaviour. *Nat. Rev. Mol. Cell Biol.* 4:446–456. http://dx.doi.org/10.1038/nrm1128

Shaw, S.K., P.S. Bamba, B.N. Perkins, and F.W. Luscinskas. 2001. Real-time imaging of vascular endothelial-cadherin during leukocyte transmigration across endothelium. *J. Immunol.* 167:2323–2330. http://dx.doi.org/10.4049/jimmunol.167.4.2323

Siddiqui, M.R., Y.A. Komarova, S.M. Vogel, X. Gao, M.G. Bonini, J. Rajasingh, Y.Y. Zhao, V. Brovkovych, and A.B. Malik. 2011. Caveolin-1–eNOS signaling promotes p190RhoGAP-A nitration and endothelial permeability. *J. Cell Biol.* 193:841–850. http://dx.doi.org/10.1083/jcb.201012129

Spindler, V., N. Schlegel, and J. Waschke. 2010. Role of GTPases in control of microvascular permeability. *Cardiovasc. Res.* 87:243–253. http://dx.doi.org/10.1093/cvr/cvq086

van Wetering, S., J.D. van Buul, S. Quik, F.P. Mul, E.C. Anthony, J.P. ten Klooster, J.G. Collard, and P.L. Hordijk. 2002. Reactive oxygen species mediate Rac-induced loss of cell-cell adhesion in primary human endothelial cells. *J. Cell Sci.* 115:1837–1846.

Wildenberg, G.A., M.R. Dohn, R.H. Carnahan, M.A. Davis, N.A. Lobdell, J. Settleman, and A.B. Reynolds. 2006. p120-catenin and p190RhoGAP regulate cell-cell adhesion by coordinating antagonism between Rac and Rho. *Cell*. 127:1027–1039. http://dx.doi.org/10.1016/j.cell.2006.09.046

Wu, Y.I., D. Frey, O.I. Lungu, A. Jaehrig, I. Schlichting, B. Kuhlman, and K.M. Hahn. 2009. A genetically encoded photoactivatable Rac controls the motility of living cells. *Nature*. 461:104–108. http://dx.doi.org/10.1038/nature08241

Yamada, S., and W.J. Nelson. 2007. Localized zones of Rho and Rac activities drive initiation and expansion of epithelial cell–cell adhesion. *J. Cell Biol.* 178:517–527. http://dx.doi.org/10.1083/jcb.200701058

Zebda, N., Y. Tian, X. Tian, G. Gawlak, K. Higginbotham, A.B. Reynolds, A.A. Birukova, and K.G. Birukov. 2013. Interaction of p190RhoGAP with C-terminal domain of p120-catenin modulates endothelial cytoskeleton and permeability. *J. Biol. Chem.* 288:18290–18299. http://dx.doi.org/10.1074/jbc.M112.432757

Zhang, Y., S. Sivasankar, W.J. Nelson, and S. Chu. 2009. Resolving cadherin interactions and binding cooperativity at the single-molecule level. *Proc. Natl. Acad. Sci. USA*. 106:109–114. http://dx.doi.org/10.1073/pnas.0811350106